Transport activity and presence of ClC-7/Ostm1 complex account for different cellular functions.

Weinert, S., Jabs, S., Hohensee, S., Chan, W.L., Kornak, U., Jentsch, T.J.

Transport activity and presence of ClC-7/Ostm1 complex account for different cellular functions

Stefanie Weinert[1,2], Sabrina Jabs[1,2], Svea Hohensee[1], Wing Lee Chan[3,4], Uwe Kornak[3,4], Thomas J. Jentsch[1,2,5,§]

[1] Leibniz-Institut für Molekulare Pharmakologie (FMP), D-13125 Berlin, Germany

[2] Max-Delbrück-Centrum für Molekulare Medizin (MDC), D-13125 Berlin, Germany

[3] Institut für Humangenetik, Charité Universitätsmedizin Berlin, D-14059 Berlin, Germany

[4] Max-Planck-Institut für Molekulare Genetik, D-14195 Berlin, Germany

[5] Neurocure Cluster of Excellence, Charité Universitätsmedizin Berlin, D-10117 Berlin, Germany

[§]Corresponding author

e-mail: Jentsch@fmp-berlin.de

Phone: +49-30-9406-2961

Fax: +49-30-9406-2960

Running title: *In vivo* structure-function of ClC-7 transporter

Key words: acidification / anion transport / grey-lethal / lysosome / Wnt signalling

Character count: 29.098 characters

Abstract

Loss of the lysosomal ClC-7/Ostm1 $2Cl^-/H^+$-exchanger causes lysosomal storage disease and osteopetrosis in humans and additionally changes fur colour in mice. Its conversion into a Cl^- conductance in *Clcn7*$^{unc/unc}$ mice entails similarly severe lysosomal storage, but less severe osteopetrosis and no change in fur colour. To elucidate the basis for these phenotypical differences, we generated *Clcn7*$^{td/td}$ mice expressing an ion transport-deficient mutant. Their osteopetrosis was as severe as in *Clcn7*$^{-/-}$ mice, suggesting that the electric shunt provided by ClC-7^{unc} can partially rescue osteoclast function. The normal coat colour of *Clcn7*$^{td/td}$ mice and their less severe neurodegeneration suggested that the ClC-7 protein, even when lacking measurable ion transport activity, is sufficient for hair pigmentation and that the conductance of ClC-7^{unc} is harmful for neurons. Our *in vivo* structure-function analysis of ClC-7 reveals that both protein-protein interactions and ion transport must be considered in the pathogenesis of ClC-7 related diseases.

Introduction

Acidic luminal pH in endosomes and lysosomes influences their trafficking, enzymatic activities and transport of substances across their limiting membranes. Luminal acidification is accomplished by electrogenic vacuolar H^+-ATPases that require an electric shunt, which in the classical model was thought to be mediated by chloride channels. Members of the CLC anion transporter gene family [1, 2], five of which reside in endosomes or lysosomes, were thought to represent these channels. However, ClC-4 through ClC-7 are rather exchangers that couple Cl^- influx to H^+ efflux [3-7]. Electrogenic Cl^-/H^+-exchange can support proton pumping [8, 9] and might be even be more efficient than Cl^- channels in supporting vesicular acidification [6]. However, lysosomal pH is normal in mice lacking ClC-7 [6, 10, 11] and the strict coupling of Cl^- flux to H^+ countertransport suggested that vesicular CLCs accumulate Cl^- into acidic compartments [12] as shown for lysosomes [6]. To clarify the relative contributions of shunt conductance and proton coupling to their biological roles, we had generated *Clcn5*$^{unc/unc}$ and *Clcn7*$^{unc/unc}$ mice in which Cl^- transport was *unc*oupled from H^+-transport by single point mutations [6, 8]. Surprisingly, these *unc* mice [6, 8] displayed *grosso modo* the same phenotypes as the respective null mice [10, 13, 14], i.e. impaired renal endocytosis in *Clcn5*$^{unc/unc}$ mice and osteopetrosis associated with a lysosomal storage disorder and neurodegeneration in *Clcn7*$^{unc/unc}$ mice (Table E1). Hence a Cl^- conductance cannot replace electrogenic Cl^-/H^+-exchange in many cellular functions.

ClC-7, together with its obligate β-subunit Ostm1 [11], is expressed in virtually all tissues [14, 15]. It localizes to late endosomes and lysosomes and is inserted into the acid-secreting ruffled border of bone-resorbing osteoclasts [10, 14]. Loss of ClC-7 function causes osteopetrosis in mice [14], humans [14, 16] and cattle [17] and entails lysosomal storage and neurodegeneration in mice [10]. Decreased proteolytical capacity of lysosomes was demonstrated in *Clcn7*$^{-/-}$ proximal tubules [18]. The unchanged steady-state pH of *Clcn7*$^{-/-}$ lysosomes [10, 11] was explained by a lysosomal cation conductance that shunts H^+-ATPase currents in parallel to ClC-7 [6, 19]. By contrast, the osteopetrosis of *Clcn7*$^{-/-}$ mice was attributed to impaired acidification of the osteoclast resorption lacuna [14]. Together with the H^+-ATPase, ClC-7 is inserted by lysosomal exocytosis into the ruffled border of osteoclasts where it may shunt H^+-ATPase currents [14]. Finally, *Clcn7*$^{-/-}$ mice display grey fur in an *agouti* background. This phenotype might be linked to

melanosomes, a lysosome-related compartment. Phenotypes virtually identical to those of *Clcn7*$^{-/-}$ mice are found in *grey-lethal* mice [11, 20] which carry a mutation in the gene encoding Ostm1.

Whereas the phenotypes of *Clcn5*$^{-/-}$ and *Clcn5*$^{unc/unc}$ mice are nearly identical, some of the phenotypes of *Clcn7*$^{-/-}$ and *Clcn7*$^{unc/unc}$ mice differ in severity [6], i.e. *Clcn7*$^{unc/unc}$ mice show less severe osteopetrosis and lack the coat colour phenotype [6, 11] (Table E1). Two hypotheses may be invoked to explain these differences. First, the shunt conductance provided by ClC-7^{unc} may suffice to support some, but not all cellular functions. Second, the difference may be owed to lacking ClC-7 protein interactions in *Clcn7*$^{-/-}$, but not in *Clcn7*$^{unc/unc}$ mice which express a correctly targeted ClC-7 mutant at normal levels [6].

Here we generated a novel *Clcn7*$^{td/td}$ mouse model that expresses a *t*ransport-*d*eficient point mutant of ClC-7. The ClC-7^{td} mutant protein neither transports Cl^- nor H^+ to a measurable degree [7], but, like ClC-7^{unc}, is expected to be fully interaction-competent. Comparative analyses of these mice suggest that a pure Cl^- conductance partially rescues the lack of Cl^-/H^+-exchange in osteoclasts, whereas normal pigmentation requires ClC-7 protein interactions, but not ClC-7 ion transport activity. Surprisingly, our study also shows that the Cl^- conductance of ClC-7^{unc} may have detrimental effects on CNS neurons.

Results

Transport-deficient ClC-7 mutant and Ostm1 are expressed normally

We generated mice in which the 'proton glutamate' E312 of ClC-7 was mutated to alanine (Figure E1) abolishing both Cl^- and H^+-transport of ClC-7/Ostm1 [7], hence our designation of this allele as '*transport-deficient*' (td). Homozygous *Clcn7*$^{td/td}$ mice were born at Mendelian ratio. Like *Clcn7*$^{unc/unc}$ and *Clcn7*$^{-/-}$ mice, they were growth retarded and most of them died within 6 weeks after birth. Surprisingly a few *Clcn7*$^{td/td}$ mice survived more than 1 year (Figure E2). The genetic background of *Clcn7*$^{td/td}$ mice cannot account for this difference as these mice were studied in comparable mixed genetic backgrounds. *Clcn7*$^{+/td}$ mice lacked an obvious phenotype. ClC-7^{td} protein levels were undistinguishable from ClC-7 levels in wild-type (WT) mice (Fig 1A,B). Like in *Clcn7*$^{unc/unc}$ mice [6], neither the abundance of Ostm1 [11], nor its

processing by lysosomal proteases was changed in *Clcn7*$^{td/td}$ mice (Fig 1A). WT ClC-7 and ClC-7^{td} similarly localized to Lamp-1 positive structures in primary fibroblasts (Fig 1C), suggesting unchanged interactions with the trafficking machinery. Ostm1 had left the endoplasmic reticulum (ER) and co-localized with ClC-7^{td} in lysosomes (Fig 1C).

Lysosomal ion homeostasis in Clcn7$^{td/td}$ mice

Because ClC-7 may contribute to a countercurrent for the vacuolar H^+-ATPase [7, 14], we measured lysosomal pH of *Clcn7*$^{td/td}$ fibroblasts and found it to be unchanged (Figure E3A). Measurements of lysosomal Cl^- concentration with a dextran-coupled Cl^--sensitive ratiometric dye [6] revealed reduced lysosomal Cl^- accumulation (Figure E3B). Both results resemble those made with *Clcn7*$^{-/-}$ and *Clcn7*$^{unc/unc}$ mice [6, 10].

Delayed neurodegeneration in Clcn7$^{td/td}$ mice

Like *Clcn7*$^{-/-}$ and *Clcn7*$^{unc/unc}$ mice, *Clcn7*$^{td/td}$ mice displayed progressive degeneration in the hippocampus (Fig 2). However, it appeared much later and was only detectable in the few surviving older mice. Neuronal cell loss was observed within the CA3 region and progressed to an almost complete loss of CA3 pyramidal cells at 10 months of age (Fig 2D,E). There was no detectable hippocampal cell loss in 4 weeks-old *Clcn7*$^{td/td}$ mice (Fig 2C). Nevertheless, pathological changes were observed, in particular in CA3 neurons and in some parts of the cortex. In those regions, lysosomal membrane proteins like Lamp-1 and ClC-7^{td} itself, were more intensely labelled and showed a broad distribution in neuronal somata rather than being stained in scattered puncta as in the WT (Fig 3A,B and Figure E4). A similar observation was made for ClC-7^{unc} (Fig 3A). Lysosomal storage was apparent 4 weeks after birth, including intracellular carbohydrate accumulation (Fig 2F) and increased levels of lysosomal acid phosphatase (Fig 2G). At P21 electron-dense osmiophilic material accumulated in lysosomal compartments of neuronal somata in the CA3 but not in the CA1 region (Fig 2H). The autophagy marker LC3-II was strongly increased in *Clcn7*$^{-/-}$ and *Clcn7*$^{unc/unc}$, but not in *Clcn7*$^{td/td}$ mice (Fig 2I). In striking contrast to the early postnatal retinal degeneration of *Clcn7*$^{-/-}$ and *Clcn7*$^{unc/unc}$ mice, retinae of 3 weeks-old (Figure E5A) and even 10 months-old *Clcn7*$^{td/td}$ mice (Figure E5B) appeared normal. The increased survival of *Clcn7*$^{td/td}$ mice thus correlated with their delayed neurodegeneration.

Osteopetrosis of ClC-7^{td} mice as severe as in ClC-7 KO

Immunolabelling of tibiae revealed that both ClC-7^{td} and its β-subunit Ostm1 were normally expressed in *Clcn7*$^{td/td}$ osteoclasts (Figure E6A). ClC-7 and ClC-7^{td} similarly co-localized with the a3 subunit of the V-type H^+-ATPase at the ruffled border (Figure E6B). Unlike the milder osteopetrosis of *Clcn7*$^{unc/unc}$ mice [6], the osteopetrosis of *Clcn7*$^{td/td}$ (Fig 4A) was as severe as in *Clcn7*$^{-/-}$ [14] or *grey-lethal* (*Ostm1*$^{-/-}$) mice [20]. Bone density was similarly increased in *Clcn7*$^{td/td}$ and *Clcn7*$^{-/-}$ mice (Fig 4C). As observed for the other ClC-7 mouse models, teeth were formed in *Clcn7*$^{td/td}$ mice but did not erupt (Fig 4B). Electron micrographs showed a partially deranged ruffled border membrane in *Clcn7*$^{td/td}$ mice (Fig 4D). Using the sealing zone, which laterally delimits the resorption lacuna between osteoclasts and bone matrix, as localization marker, we categorized ruffled borders *in situ* as absent, immature or mature (Fig 4D,E). 20% of osteoclasts from *Clcn7*$^{-/-}$ and *Clcn7*$^{td/td}$ mice totally lacked a ruffled border and only about 40% showed a mature ruffled border (Fig 4E). All osteoclasts from *Clcn7*$^{unc/unc}$ mice formed ruffled border membranes, of which 70% appeared mature. Hence the severity of osteopetrosis correlates with an impairment of ruffled border formation.

Coat colour phenotype is absent in ClC-7^{td} mice

The pigments of hair and skin are synthesized in melanosomes, a lysosome-related compartment of melanocytes, and are then transferred to keratinocytes. The grey fur of *Clcn7*$^{-/-}$ or *Ostm1*$^{-/-}$ mice [14, 20] thus agrees with the lysosomal localization of ClC-7/Ostm1. Surprisingly, the fur colour was changed neither in *Clcn7*$^{unc/unc}$ [6] nor in *Clcn7*$^{td/td}$ mice (Fig 5A) which express mutant full-length ClC-7 proteins that display or lack, respectively, a Cl^- conductance. The *agouti* gene modulates the colour of the hair shaft, resulting in a band of yellow (owed to pheomelanin granules) in the otherwise dark (eumelanin) pigmented hair shaft. The pigment in the yellow band was clumped and reduced in *Clcn7*$^{-/-}$ and *Ostm1*$^{-/-}$ (*gl*) mice whereas eumelanin granules were unchanged in their dark hair shafts (Fig 5B). Hair shaft pigmentation of *Clcn7*$^{unc/unc}$ and *Clcn7*$^{td/td}$ mice was unchanged compared to WT (Fig 5B).

Activation of Wnt signalling in primary fibroblasts and melanocytes

Melanocyte differentiation depends on Wnt signalling [21] and Ostm1 has been proposed to play a role in the canonical Wnt pathway [22] although the molecular mechanism remains obscure. Because the Ostm1 protein is absent or severely reduced in *Ostm1*$^{-/-}$ and *Clcn7*$^{-/-}$ mice, respectively [11], but unchanged in *Clcn7*$^{unc/unc}$ [6] and *Clcn7*$^{td/td}$ mice, we asked whether the difference in coat colour might be due to differences in Wnt signalling. Primary fibroblasts from WT, *Clcn7*$^{-/-}$ and *Ostm1*$^{-/-}$ mice were exposed to Wnt3a to activate canonical Wnt signalling and mRNA levels of the target gene axin2 [23] were determined. Basal and Wnt3-stimulated Axin2 expression was unchanged in *Clcn7*$^{-/-}$ and *gl* (*Ostm1*$^{-/-}$) fibroblasts (Figure E7A,B) and in *Clcn7*$^{-/-}$ melanocytes (Figure E7C) compared to WT. Hence differential activation of the Wnt signalling pathway is unlikely to contribute to the phenotypical differences of the present *Clcn7* mouse models.

Discussion

Our analysis of *Clcn7*$^{td/td}$, *Clcn7*$^{-/-}$ and *Clcn7*$^{unc/unc}$ mice [6, 14] represents a novel *in vivo* structure-function analysis of ClC-7/Ostm1 that complements similar *in vitro* studies focusing on biophysical properties [7, 24]. Comparison of the pathologies of these mice (Table E1) yielded a surprisingly complex picture of the roles of ClC-7 in lysosome, osteoclast and melanocyte biology. Phenotypes resulting from *Clcn7* mutations cannot be assigned exclusively to a loss of ion transport activity.

As vesicular CLCs may shunt proton pump currents in the endolysosomal system and at the osteoclast resorption lacuna [2, 8, 9, 14], we assumed that a similar shunt by the ClC-7^{unc} Cl^- conductance may rescue some of the pathologies of *Clcn7*$^{-/-}$ mice. Comparison of the present *Clcn7*$^{td/td}$ with *Clcn7*$^{-/-}$ and *Clcn7*$^{unc/unc}$ mice showed that this holds true for osteopetrosis, but not for the changed fur colour or neurodegeneration. The severity of osteopetrosis, which is less severe in *Clcn7*$^{unc/unc}$ mice than in the other two mouse models, correlated with the malformation of the ruffled border. Hence the formation of this acid-secreting membrane does not only require the presence of the ClC-7/Ostm1 protein complex, but also its ion transport activity. A Cl^- conductance can only partially substitute for $2Cl^-/H^+$-exchange in osteoclast function.

Surprisingly, normal hair pigmentation did not require ClC-7/Ostm1 ion transport, but just the presence of the protein complex (Table E1). Comparison of *Clcn7*$^{td/td}$ with *Clcn7*$^{-/-}$ mice showed that the ion transport-deficient ClC-7^{td}/Ostm1 complex was also beneficial for neurons, but did not suffice to prevent lysosomal storage and CNS degeneration. Comparing *Clcn7*$^{td/td}$ with *Clcn7*$^{unc/unc}$ mice, both of which express correctly targeted ClC-7/Ostm1, revealed a detrimental effect of the ClC-7^{unc} Cl^- conductance on neurons, in stark contrast to its positive influence on osteoclasts. A toxic effect of the ClC-7^{unc} conductance on neurons is also indicated by the fact that heterozygous *Clcn7*$^{+/unc}$, but not *Clcn7*$^{+/-}$ mice, display neurodegeneration [6]. In all three genotypes (*Clcn7*$^{-/-,\ unc/unc,\ or\ td/td}$), lysosomal pH is normal and lysosomal Cl^- concentrations are similarly decreased [6], eliminating these parameters as explanations for differences in lysosomal pathology. However, there may be differential effects on lysosomal voltage that may influence transmembrane transport processes and possibly membrane budding and fusion. Reductionist model calculations predict a lumen-positive potential (~20 mV) with a Cl^- channel, but a lumen-negative potential with a $2Cl^-/H^+$-exchanger [6]. Moreover, the ClC-7 *unc* mutation (E245A) [7] not only uncouples Cl^-- from H^+-transport, but also abolishes voltage- and time-dependent gating [3-5, 7, 24-26]. WT ClC-7 almost lacks transport activity at cytoplasmic negative (i.e. lumen-positive) potentials. Currents increase steeply when cytoplasmic voltage exceeds ~+20 mV [7]. Hence the *unc* mutation will robustly increase steady-state ClC-7 currents in lysosomes. Moreover, the slow gating of WT ClC-7/Ostm1 [7] would prevent a full activation of ClC-7 during transient inside-negative voltage excursions that may occur e.g. upon NAADP-induced Ca^{2+} release [27, 28]. Intriguingly many pathogenic *CLCN7* mutations [7, 17, 29] accelerate ClC-7/Ostm1 gating, suggesting that early exchange currents may be pathogenic. ClC-7^{unc} currents respond instantaneously to voltage and may thus be more harmful than those from accelerating mutants expressed in patients.

The beneficial effect of ClC-7^{td}/Ostm1 on melanocytes and neurons raises the question whether it is totally transport-deficient as assumed above. We cannot exclude that the mutant mediates currents below our detection limit of about 3% of WT. If small currents remain in ClC-7^{td} mutants they likely resemble ClC-7^{unc} currents because similar mutations in EcClC-1 convert this bacterial $2Cl^-/H^+$-exchanger into a pure Cl^- conductance [30]. As ClC-7^{unc} currents are detrimental for neurons we

conclude that indeed the ClC-7^{td}/Ostm1 complex itself, and not a putative ion transport activity, is beneficial for neurons and by extension for melanocytes. Identifying novel binding partners for ClC-7/Ostm1 that may explain these beneficial effects is a daunting task for future investigations.

Material & Methods

Detailed methods can be found in the Expanded View.

Mice

Clcn7$^{-/-}$[14] and *Clcn7*$^{unc/unc}$ mice [6] have been described. *Grey-lethal* (*Ostm1*$^{-/-}$) mice [20] were from Jackson Laboratories. *Clcn7*$^{td/td}$ mice were generated by homologous recombination using a construct in which the E312A mutation was inserted into Exon 11 of *Clcn7.* Animals were housed under standard conditions in the MDC animal facility according to institutional guidelines and kept on a 12 h light/dark cycle. LAGeSo, Berlin, Germany, approved all experimental procedures.

Antibodies

Find primary antibodies in the Expanded View Table E2. Secondary antibodies were coupled to Alexa Fluor 488, 546 (Invitrogen) or HRP (Jackson ImmunoResearch).

Membrane preparation, tissue homogenates and immunoblot

Brain extracts were prepared from adult mice, blotted on PVDF membrane and probed according to standard procedures.

Histology and electron microscopy

Sections were stained with H&E, Nissl, periodic acid Schiff reagent (PAS), indicated antibodies and for lysosomal acid phosphatase activity. For EM, mice were perfused with 4% (w/v) PFA and 2.5% (v/v) glutaraldehyde in 0.1 M phosphate buffer (pH 7.4). 150-µm sagittal sections were prepared with a vibratome. Slices were postfixed in 2% (v/v) OsO_4, dehydrated and embedded in epon. Semi-thin sections (0.5 µm) were labelled with toluidine blue. Ultrathin sections (60 nm) were stained with uranyl acetate and lead citrate.

Micro-computed tomography (CT)

PFA-fixed tibiae were analyzed with a Skyscan 1172 µCT (Bruker-MicroCT) at 7 µm resolution. A ROI of 350 µm situated 200 µm below the growth plate comprising the secondary spongiosa was evaluated using the CTAn software with a lower grey

threshold of 30 (Bruker-MicroCT). 3D reconstruction was done by the AMIRA software package (Visualization Sciences Group).

WNT stimulation of primary cells

Primary fibroblasts were starved >6h in DMEM containing 0.1% (w/v) BSA and stimulated with 80 ng/ml recombinant murine (rm) Wnt-3A (CF, R&D Systems) overnight in growth medium. Melanocytes were starved overnight in MEM Eagle containing 0.1% BSA and stimulated overnight with 80 ng/mL rmWnt-3A in MEM Eagle containing 10% (v/v) FBS (all Pan-Biotech) and 200 nM TPA.

Determination of lysosomal pH

Lysosomal pH was measured by ratiometric fluorescence imaging of the pH sensor Oregon Green dextran 488 (Invitrogen) as described [6].

Determination of relative lysosomal chloride concentrations

Lysosomal chloride was measured by ratiometric fluorescence live cell imaging of MEQ/TMR-dextran [6].

Acknowledgements

We thank M. Richter (FMP) for synthesizing the dextran-coupled Cl^- indicator, K. Räbel and A. von Bock for technical assistance, and H.J. Kaiser for writing the Fiji plug-in for the evaluation of lysosomal pH. Supported, in part, by grants from the Deutsche Forschungsgemeinschaft (JE164/7, JE164/9, SFB740 TP C5), an Advanced Investigator Grant from the European Research Council (*ERC Grant Agreement n. 294435)* and the Prix Louis-Jeantet de Médecine to TJJ.

Author Contributions

SW generated knock-in mice, performed biochemical experiments, immunohistochemistry and measured lysosomal pH, SJ measured lysosomal [Cl^-] and investigated Wnt signalling, SH performed electron microscopy, UK and WLC µ-CT and bone characterization, TJJ planned the study, and TJJ, SW, and SJ wrote the paper.

Conflict of Interest

The authors declare no conflict of interest.

Figure legends

Figure 1 — Normal expression of ClC-7^{td} and Ostm1 in *Clcn7*$^{td/td}$ mice.

A ClC-7 and Ostm1 immunoblots of brain membranes. ClC-7 was drastically reduced in *grey-lethal* (gl) mice. Only the Ostm1 precursor Ostm1^{P} (filled arrow) is present in *Clcn7*$^{-/-}$ tissue. Ostm1^{m}, mature form (open arrow). Actin, loading control. Asterisk, non-specific band.

B Quantification of ClC-7 immunoblots (normalized to actin).

C Co-immunostaining of ClC-7 (green) with Lamp-1 (red, upper panels) or Ostm1 (red, lower panels) in primary fibroblasts. ClC-7^{td} and Ostm1 co-localize in Lamp-1-positive structures. DNA stained with DAPI (upper panels). Asterisks, non-specific immunoreactivity in the nucleus (scale bar: 20 µm).

Figure 2 — Brain pathology of *Clcn7*$^{td/td}$ mice.

A-C Neuronal cell loss (arrowheads) in hippocampal CA3 region of *Clcn7*$^{-/-}$ but not of *Clcn7*$^{td/td}$ mice (Nissl staining).

D,E Incipient (D) and complete (E) CA3 neurodegeneration (arrowheads) of 5 months- and 10 months-old *Clcn7*$^{td/td}$ mice, respectively. Right panels: higher magnification not necessarily of section shown at left. (scale bars: left, 400 µm; right, 100 µm).

F Strong PAS staining (arrowheads) in P28 CA3 neurons of *Clcn7*$^{td/td}$ but not of WT mice (scale bar: 100 µm).

G Increased lysosomal acid phosphatase activity in cortex of P28 *Clcn7*$^{td/td}$ mice compared to WT (scale bar: 100 µm).

H Lysosomal storage material in CA3 pyramidal neuron somata shown by electron microscopy (N, nucleus; dotted line around soma). Right: higher magnification of a soma different from that at left (scale bars: left: 2 µm, right: 1 µm).

I Immunoblots showed increase of the autophagic marker LC3-II in brain of 3-week old *Clcn7*$^{-/-}$ and *Clcn7*$^{unc/unc}$ vs. *Clcn7*$^{td/td}$ and WT mice. Actin, loading control. Right panel: Quantification of immunoblots normalized to actin and LC3-I.

Figure 3 — Abnormal lysosomal morphology in ClC-7 mouse models.

A ClC-7 immunolabelling in somata of CA1 and CA3 pyramidal and of cortical neurons in *Clcn7*$^{unc/unc}$, *Clcn7*$^{td/td}$ and WT mice. ClC-7^{td} is abnormal in the CA3 region and partially in the cortex. Increased labelling intensity suggests larger ClC-7 amounts in *Clcn7*$^{td/td}$ CA3, and in *Clcn7*$^{unc/unc}$ CA3, CA1, and cortex (scale bar: 10 µm; PC, purkinje cells).

B Abnormal Lamp-1 distribution in cortical and CA3 (arrowheads), but not CA1 neurons of 10 months-old *Clcn7*$^{td/td}$ mice. DNA stained with DAPI (scale bar: 10 µm).

Figure 4 — Osteopetrosis in *Clcn7*$^{td/td}$ mice.

A Micro-CT revealed similar osteopetrosis of tibiae of 3 weeks-old *Clcn7*$^{-/-}$ and *Clcn7*$^{td/td}$ mice (scale bar: 1 mm).

B Micro-CT image of skull from P22 *Clcn7*$^{td/td}$ mouse showed impaired tooth eruption (scale bar: 10 mm).

C Similarly increased bone volume fraction of proximal tibia metaphyseal trabecular bone in *Clcn7*$^{td/td}$ mice and *Clcn7*$^{-/-}$ mice. BV, bone volume; TV, tissue volume. Student's t-test was applied; n.s., not significant.

D Electron microscopy showed mature, immature and lacking ruffled borders of *Clcn7*$^{td/td}$ osteoclasts despite the presence of a sealing zone (SZ). Arrows point at ruffled borders (scale bar: 5 µm) (Bo= bone; N=nucleus).

E Percentage of WT, *Clcn7*$^{unc/unc}$, *Clcn7*$^{td/td}$, *Clcn7*$^{-/-}$ osteoclasts exhibiting absent, immature, or mature ruffled borders. Error bars denote s.e.m..

Figure 5 — ClC-7^{td} mice lack a coat colour phenotype.

A *Clcn7*$^{td/td}$ mice are brown contrasting with the grey fur of *Clcn7*$^{-/-}$ mice.

B Upper panels: pheomelanin granules clump in hair shafts of *Clcn7*$^{-/-}$ and *Ostm1*$^{-/-}$ but not in *Clcn7*$^{unc/unc}$, *Clcn7*$^{td/td}$ and WT mice. Normally distributed eumelanin granules in the dark hair shafts of all mouse models (lower panels).

References

1. Jentsch TJ (2008) CLC chloride channels and transporters: From genes to protein structure, pathology and physiology. *Crit Rev Biochem Mol Biol* 43: 3-36
2. Stauber T, Weinert S, Jentsch TJ (2012) Cell biology and physiology of CLC chloride channels and transporters. *Compr Physiol* 2: 1701-1744
3. Scheel O, Zdebik A, Lourdel S, Jentsch TJ (2005) Voltage-dependent electrogenic chloride proton exchange by endosomal CLC proteins. *Nature* 436: 424-427
4. Picollo A, Pusch M (2005) Chloride / proton antiporter activity of mammalian CLC proteins ClC-4 and ClC-5. *Nature* 436: 420-423
5. Neagoe I, Stauber T, Fidzinski P, Bergsdorf EY, Jentsch TJ (2010) The late endosomal CLC-6 mediates proton/chloride countertransport in heterologous plasma membrane expression. *J Biol Chem* 285: 21689-21697
6. Weinert S *et al* (2010) Lysosomal pathology and osteopetrosis upon loss of H^+-driven lysosomal Cl^- accumulation *Science* 328: 1401-1403
7. Leisle L, Ludwig CF, Wagner FA, Jentsch TJ, Stauber T (2011) ClC-7 is a slowly voltage-gated $2Cl^-/1H^+$-exchanger and requires Ostm1 for transport activity. *EMBO J* 30: 2140-2152
8. Novarino G, Weinert S, Rickheit G, Jentsch TJ (2010) Endosomal chloride-proton exchange rather than chloride conductance is crucial for renal endocytosis. *Science* 328: 1398-1401
9. Günther W, Piwon N, Jentsch TJ (2003) The ClC-5 chloride channel knock-out mouse - an animal model for Dent's disease. *Pflügers Arch* 445: 456-462
10. Kasper D *et al* (2005) Loss of the chloride channel ClC-7 leads to lysosomal storage disease and neurodegeneration. *EMBO J* 24: 1079-1091
11. Lange PF, Wartosch L, Jentsch TJ, Fuhrmann JC (2006) ClC-7 requires Ostm1 as a β-subunit to support bone resorption and lysosomal function. *Nature* 440: 220-223
12. Jentsch TJ (2007) Chloride and the endosomal-lysosomal pathway: emerging roles of CLC chloride transporters. *J Physiol* 578: 633-640
13. Piwon N, Günther W, Schwake M, Bösl MR, Jentsch TJ (2000) ClC-5 Cl^--channel disruption impairs endocytosis in a mouse model for Dent's disease. *Nature* 408: 369-373
14. Kornak U, Kasper D, Bösl MR, Kaiser E, Schweizer M, Schulz A, Friedrich W, Delling G, Jentsch TJ (2001) Loss of the ClC-7 chloride channel leads to osteopetrosis in mice and man. *Cell* 104: 205-215
15. Brandt S, Jentsch TJ (1995) ClC-6 and ClC-7 are two novel broadly expressed members of the CLC chloride channel family. *FEBS Lett* 377: 15-20
16. Cleiren E *et al* (2001) Albers-Schönberg disease (autosomal dominant osteopetrosis, type II) results from mutations in the *ClCN7* chloride channel gene. *Hum Mol Genet* 10: 2861-2867
17. Sartelet A *et al* (2013) A missense mutation accelerating the gating of the lysosomal Cl^-/H^+-exchanger ClC-7/Ostm1 causes osteopetrosis with gingival hamartomas in cattle. *Dis Model Mech*, 10.1242/dmm.012500
18. Wartosch L, Fuhrmann JC, Schweizer M, Stauber T, Jentsch TJ (2009) Lysosomal degradation of endocytosed proteins depends on the chloride transport protein ClC-7. *FASEB J* 23: 4056-4068
19. Steinberg BE, Huynh KK, Brodovitch A, Jabs S, Stauber T, Jentsch TJ, Grinstein S (2010) A cation counterflux supports lysosomal acidification. *J Cell Biol* 189: 1171-1186
20. Chalhoub N, Benachenhou N, Rajapurohitam V, Pata M, Ferron M, Frattini A, Villa A, Vacher J (2003) Grey-lethal mutation induces severe malignant autosomal recessive osteopetrosis in mouse and human. *Nat Med* 9: 399-406
21. Goding CR (2000) Mitf from neural crest to melanoma: signal transduction and transcription in the melanocyte lineage. *Genes Dev* 14: 1712-1728
22. Feigin ME, Malbon CC (2008) OSTM1 regulates β-catenin/Lef1 interaction and is required for Wnt/β-catenin signaling. *Cell Signal* 20: 949-957
23. Jho EH, Zhang T, Domon C, Joo CK, Freund JN, Costantini F (2002) Wnt/beta-catenin/Tcf signaling induces the transcription of Axin2, a negative regulator of the signaling pathway. *Mol Cell Biol* 22: 1172-1183

24. Ludwig CF, Ullrich F, Leisle L, Stauber T, Jentsch TJ (2013) Common Gating of Both CLC Transporter Subunits Underlies Voltage-dependent Activation of the $2Cl^-/1H^+$ Exchanger ClC-7/Ostm1. *J Biol Chem* 288: 28611-28619
25. Friedrich T, Breiderhoff T, Jentsch TJ (1999) Mutational analysis demonstrates that ClC-4 and ClC-5 directly mediate plasma membrane currents. *J Biol Chem* 274: 896-902
26. Bergsdorf EY, Zdebik AA, Jentsch TJ (2009) Residues important for nitrate/proton coupling in plant and mammalian CLC transporters. *J Biol Chem* 284: 11184-11193
27. Calcraft PJ *et al* (2009) NAADP mobilizes calcium from acidic organelles through two-pore channels. *Nature* 459: 596-600
28. Jha A, Ahuja M, Patel S, Brailoiu E, Muallem S (2014) Convergent regulation of the lysosomal two-pore channel-2 by Mg^{2+}, NAADP, PI(3,5)P2 and multiple protein kinases. *EMBO J* 33: 501-511
29. Barvencik F *et al* (2013) *CLCN7* and *TCIRG1* mutations differentially affect bone matrix mineralization in osteopetrotic individuals. *J Bone Miner Res*, 10.1002/jbmr.2100
30. Accardi A, Walden M, Nguitragool W, Jayaram H, Williams C, Miller C (2005) Separate ion pathways in a Cl^-/H^+ exchanger. *J Gen Physiol* 126: 563-570

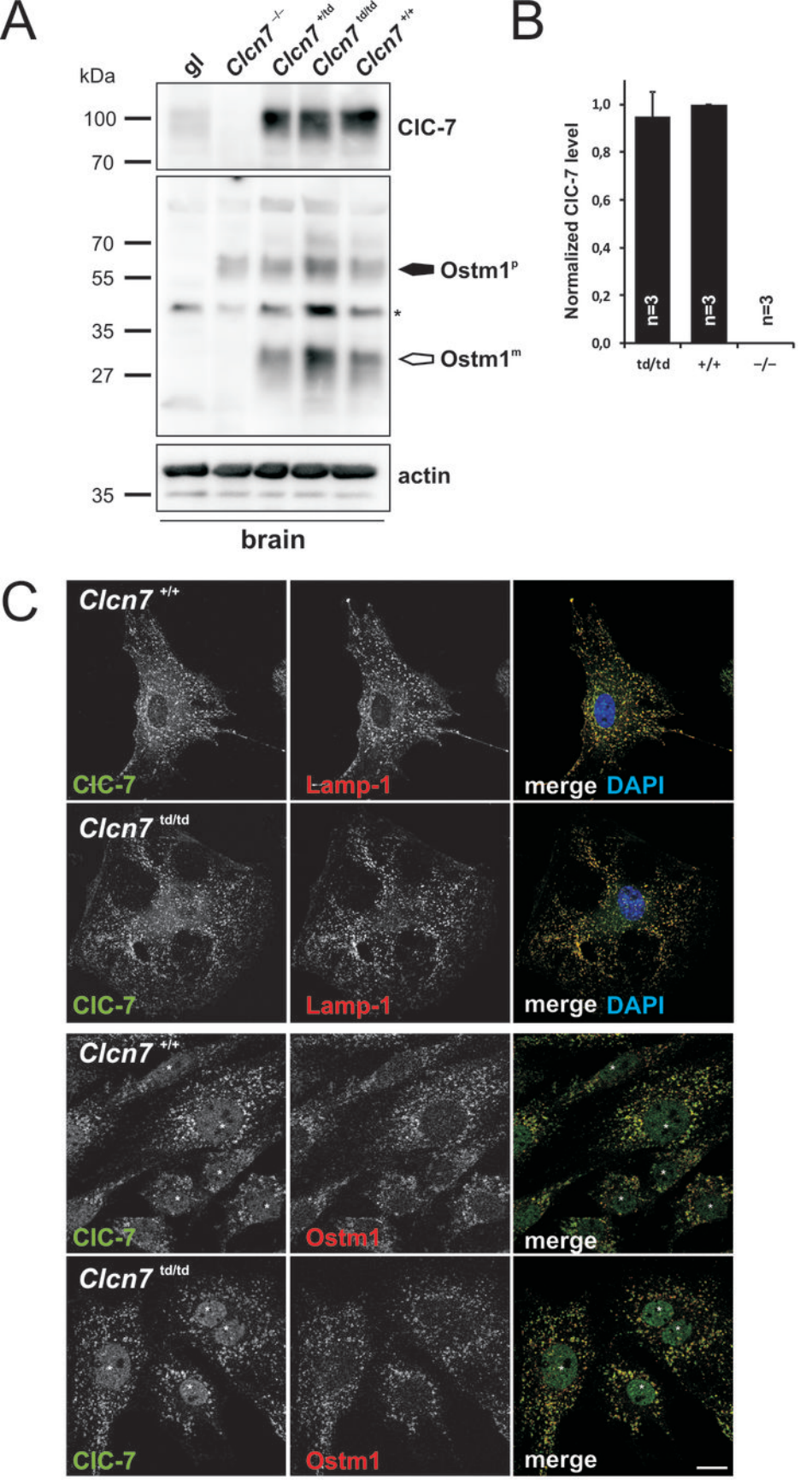
A
gl
Clcn7 −/−
Clcn7 +/td
Clcn7 td/td
Clcn7 +/+
kDa
100
70
CIC-7
70
55
35
27
Ostm1p
*
Ostm1m
35
actin
brain
B
Normalized CIC-7 level
1,0
0,8
0,6
0,4
0,2
0,0
n=3
n=3
n=3
td/td
+/+
−/−
C
Clcn7 +/+
CIC-7
Lamp-1
merge DAPI
Clcn7 td/td
CIC-7
Lamp-1
merge DAPI
Clcn7 +/+
CIC-7
Ostm1
merge
Clcn7 td/td
CIC-7
Ostm1
merge

Figure 1

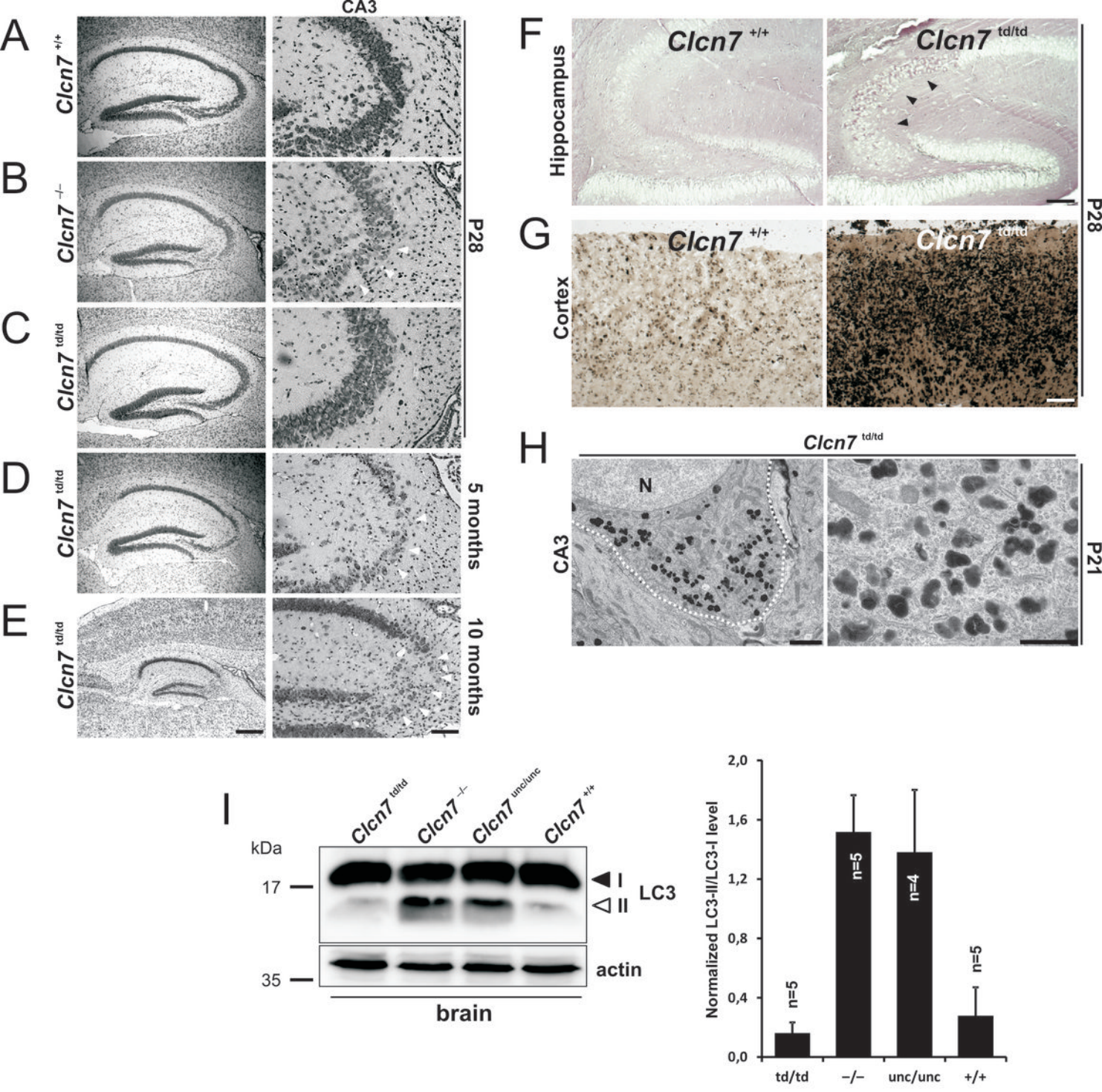
A
B
C
D
E
CA3
Clcn7 +/+
Clcn7 −/−
Clcn7 td/td
Clcn7 td/td
Clcn7 td/td
P28
5 months
10 months
F
Hippocampus
Clcn7 +/+
Clcn7 td/td
P28
G
Cortex
Clcn7 +/+
Clcn7 td/td
H
Clcn7 td/td
N
CA3
P21
I
kDa
Clcn7 td/td
Clcn7 −/−
Clcn7 unc/unc
Clcn7 +/+
17
35
I
II
LC3
actin
brain
Normalized LC3-II/LC3-I level
2,0
1,6
1,2
0,8
0,4
0,0
n=5
n=5
n=4
n=5
td/td
−/−
unc/unc
+/+

Figure 2

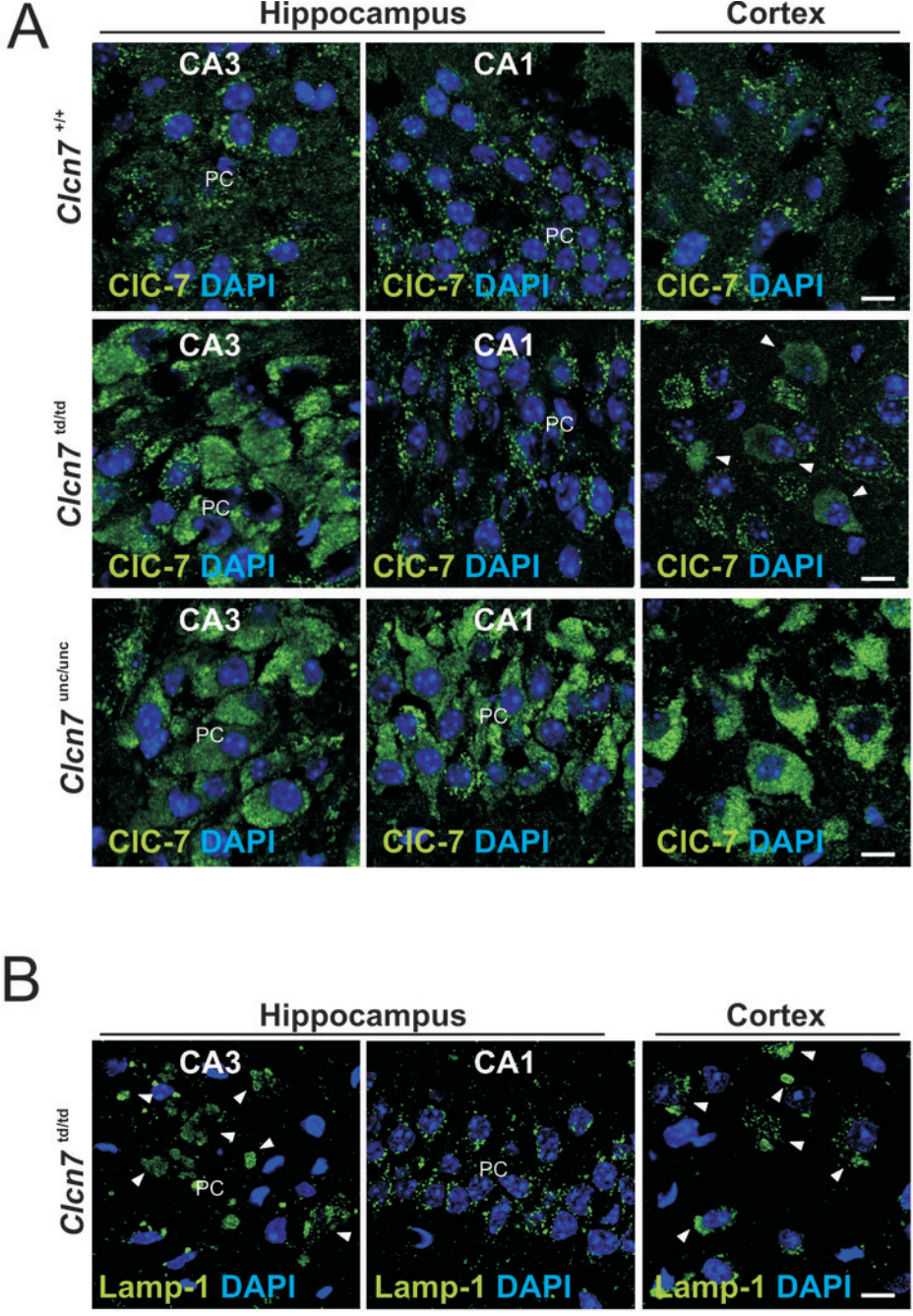
A
Hippocampus
Cortex
CA3
CA1
PC
CIC-7 DAPI
Clcn7 +/+
Clcn7 td/td
Clcn7 unc/unc
B
Lamp-1 DAPI
10 months

Figure 3

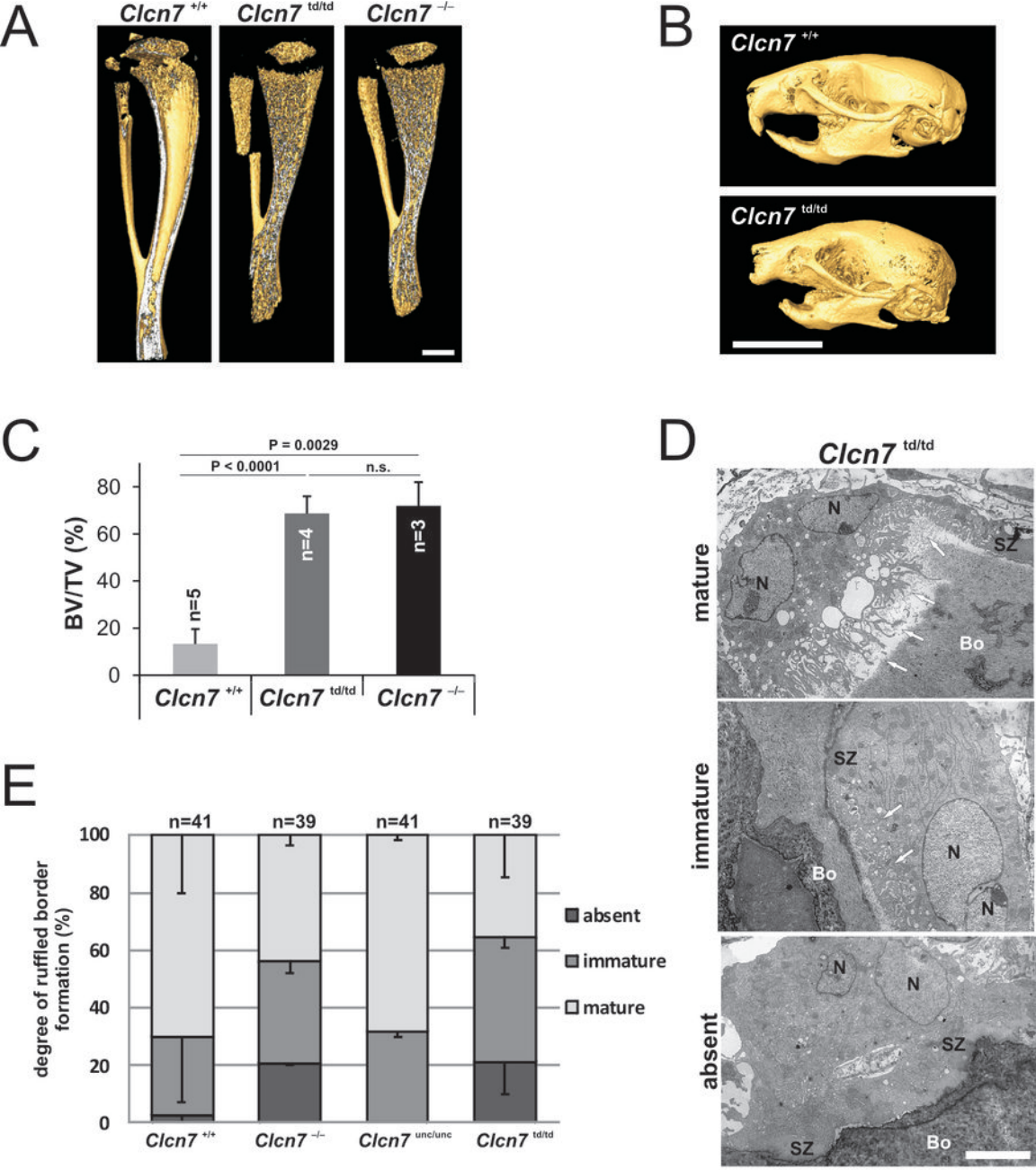
A
Clcn7 +/+
Clcn7 td/td
Clcn7 −/−
B
Clcn7 +/+
Clcn7 td/td
C
P = 0.0029
P < 0.0001
n.s.
BV/TV (%)
0
20
40
60
80
n=5
n=4
n=3
Clcn7 +/+
Clcn7 td/td
Clcn7 −/−
D
Clcn7 td/td
mature
immature
absent
N
SZ
Bo
E
n=41
n=39
n=41
n=39
degree of ruffled border formation (%)
0
20
40
60
80
100
absent
immature
mature
Clcn7 +/+
Clcn7 −/−
Clcn7 unc/unc
Clcn7 td/td

Figure 4

A

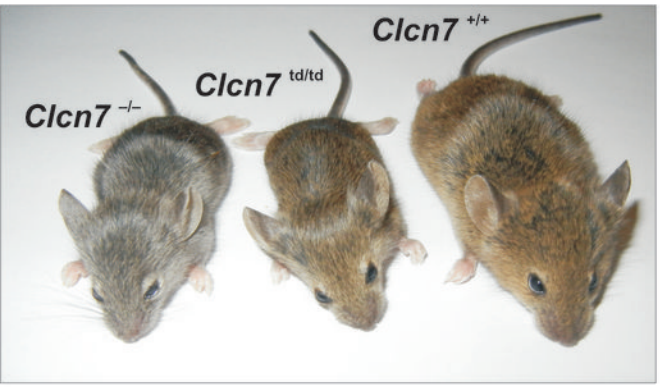
Clcn7 −/−
Clcn7 td/td
Clcn7 +/+

B

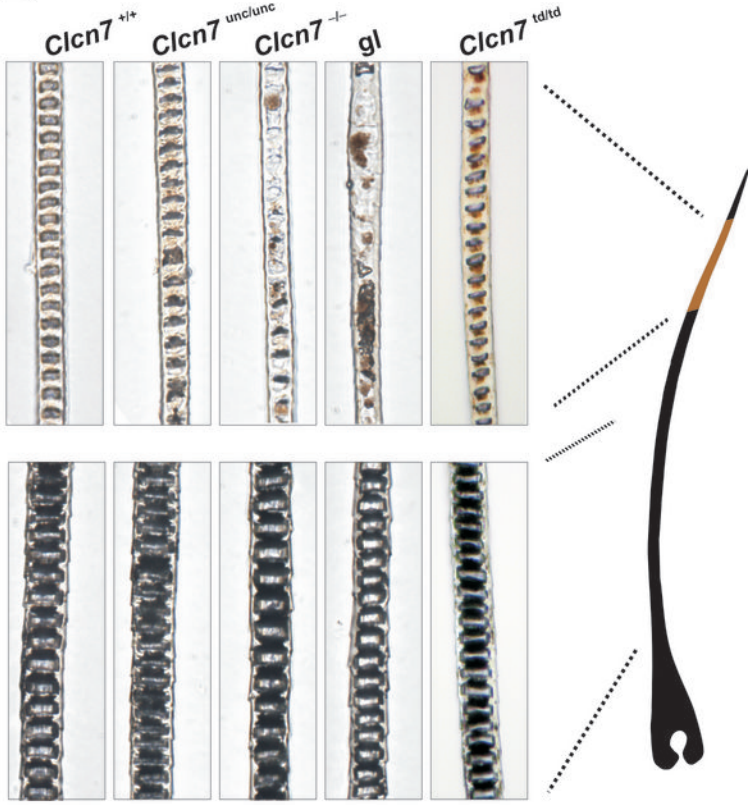
Clcn7 +/+
Clcn7 unc/unc
Clcn7 −/−
gl
Clcn7 td/td

Figure 5

Expanded View to Weinert *et al*.

Tables

Table I. Overview of features of our ClC-7 mouse models studied previously and in this study.
Green symbols indicate normal properties and red symbols abnormal (pathological) ones. n, normal. Down arrow indicate quantitatively decreased values.

Table I.

	Clcn7 $^{+/+}$	*Clcn7* $^{unc/unc}$	*Clcn7* $^{td/td}$	*Clcn7* $^{-/-}$
Intact protein	+	+	+	–
Electric shunt	+	+	–	–
Cl^-/H^+-exchange	+	–	–	–
Survival	+	–	–(+)	–
Lysosomal pathology	–	++	+	++
Lysosomal pH	n	n	n	n
Lysosomal $[Cl^-]$	n	↓	↓	↓
Osteopetrosis	–	+	++	++
Pigmentation defect	–	–	–	++

Table II. Antibodies used in this study. rb, rabbit; gp guinea pig; IHC, immunohistochemistry; ICC, immunocytochemistry; WB, western blot.

Table II.

	species	source	IHC	ICC	WB
Anti-ClC-7	rb, gp	Kornak et al, 2001	1:100	1:300	1:500
Anti-Ostm1	rb, gp	Lange et al, 2006	1:50	1:150	1:200
Anti-Lamp-1	rb	abcam, # ab24170	1:300	—	—
Anti-Lamp-1	rat	BD Bioscience, # 553792	1:100	1:200	—
Anti-a3 (V- ATPase)	gp	Lange et al, 2006	1:100	—	—
Anti-Actin	rb	Sigma-Aldrich, # A-2066	—	—	1:1000
Anti-LC3	rat	Abgent, # AP1802a	—	—	1:300

Table III. Number of animals/cell lines used for experiments.

Table III.

	number
Figure 1C	3 (+/+,td/td) independent cell lines
Figure 2 A-C	4 (+/+,td/td) animals
Figure 2 D-H	2 (+/+,td/td) animals
Figure 3 A	3 (+/+,td/td,unc/unc) animals
Figure 3 B	2 (td/td) animals
Figure 4 A	5 (+/+), 4 (td/td), 3(–/–) animals
Figure 4 B	2 (+/+,td/td) animals
Figure 4 D,E	2 (+/+,td/td,unc/unc,–/–) animals
Figure 5 A,B	3 (+/+,td/td) animals
Figure E5 A	2 (+/+,td/td,unc/unc,–/–) animals
Figure E5 B	2 (+/+,td/td) animals
Figure E6 A,B	2 (+/+,td/td) animals

Figures

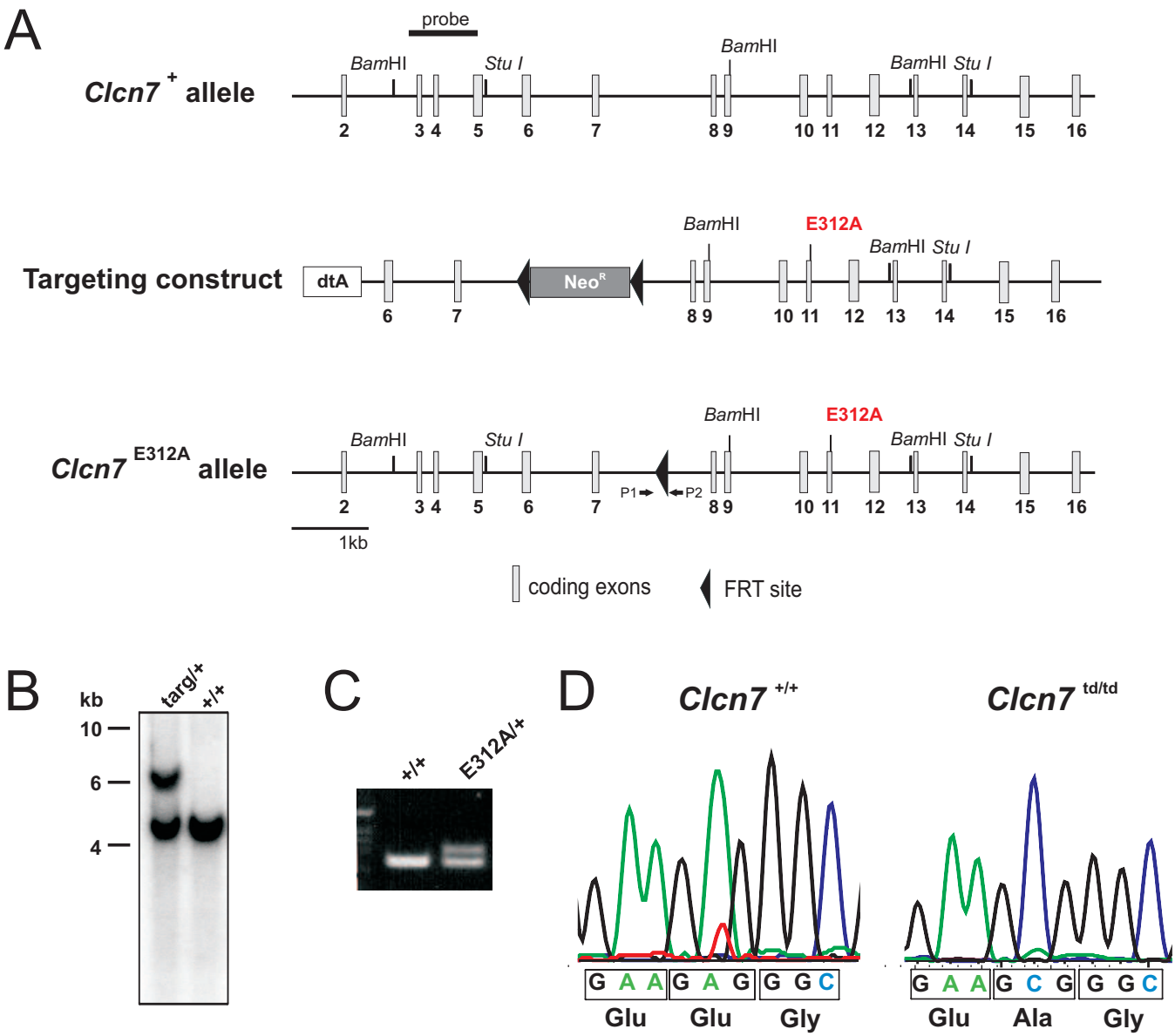

Figure E1. Generation of *Clcn7*$^{td/td}$ mice. (**A**) Gene targeting strategy. Targeting construct contains 8 kb of mouse genomic sequence encompassing exon 6 through 16 with a dtA (diphtheria toxin A) cassette added to one end to select for homologous recombination. We modified Exon 11 by introducing the E312A mutation and inserted a neomycin (Neo^{R}) resistance cassette (flanked by FRT sites) between exons 7 and 8 as selection marker. Correctly targeted embryonic stem (ES) cells were injected into blastocysts. Chimeric animals were crossed with FLPe-recombinase-expressing 'deleter' mice (Rodríguez et al, 2000) resulting in the *Clcn7*^{E312A} allele (bottom). (**B**) Mouse genomic ES cell DNA was digested with *Bam*HI for Southern blot analysis. Positive clones were identified with an external hybridization probe shown in (A). (**C**) PCR on mouse genomic DNA was used for genotyping. The sequences of PCR primers shown in (A) were for P1: 5' TATCTCAGAAGGCAGGTAGG 3' and for P2: 5' AGTCTGTTAGCCAGAGGTAG 3'. (**D**) DNA sequence obtained from homozygous *Clcn7*$^{td/td}$ mice confirmed the presence of the E312A mutation.

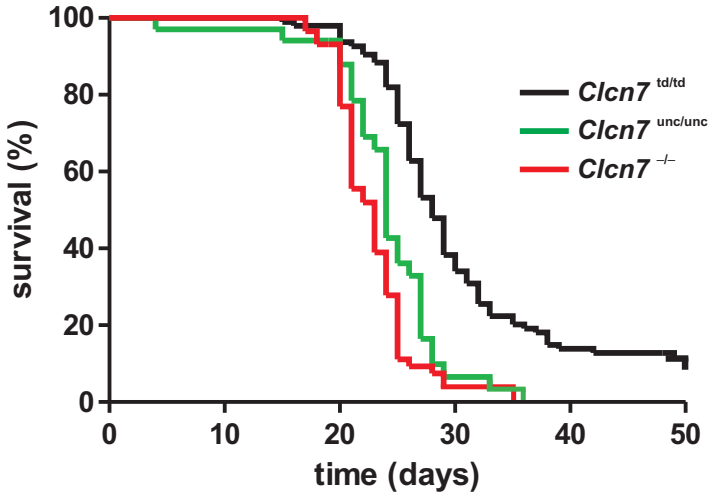

Figure E2. Survival rates of ClC-7 mouse models. *Clcn7*$^{unc/unc}$ and *Clcn7*$^{-/-}$ mice died within 3-4 weeks after birth, whereas *Clcn7*$^{td/td}$ mice died on average a few days later. Intriguingly, some *Clcn7*$^{td/td}$ mice survived for more than 2 months and even got older than 10 months (*Clcn7*$^{td/td}$, n = 103, *Clcn7*$^{-/-}$, n = 61 and *Clcn7*$^{unc/unc}$, n = 35).

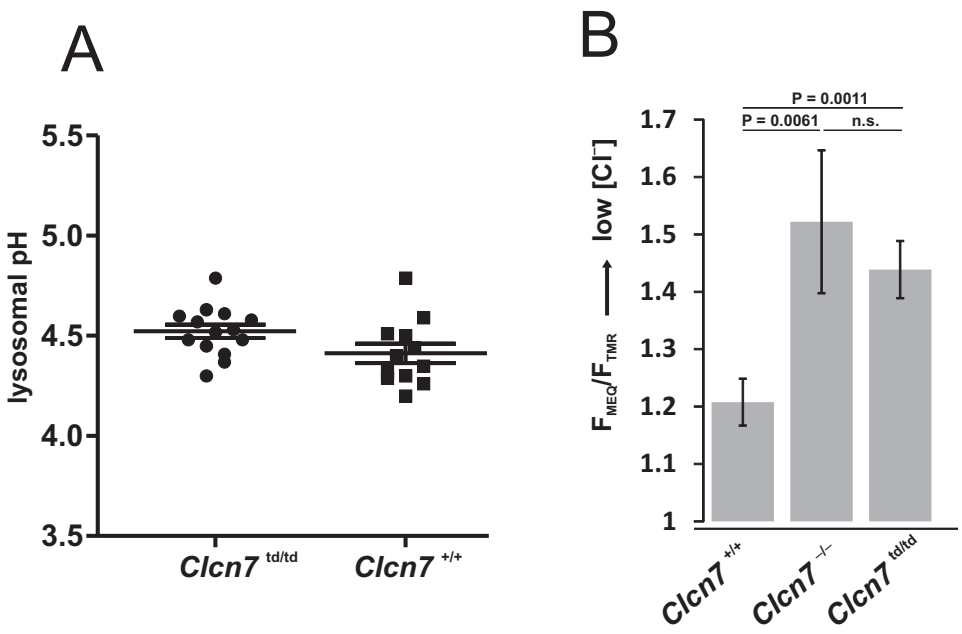

Figure E3. Ion homeostasis in lysosomes in ClC-7 mouse models. (**A**) No significant difference in steady-state lysosomal pH between *Clcn7*$^{td/td}$ and *Clcn7*$^{+/+}$ fibroblasts as measured by Oregon Green dextran fluorescence in 3 independent cell lines and 15 (td/td) and 11 (+/+) dishes. Lines show mean ± s.e.m. of the individual measurements that are depicted as dots and squares. (**B**) Lysosomal chloride concentration was reduced in *Clcn7*$^{td/td}$ compared to WT lysosomes as measured by fluorescence ratio of MEQ over TMR, which were coupled to dextran. Cells were preincubated in low Cl^- saline to shift $[Cl^-]_{lys}$ into the useful measuring range. Means (n=12 for WT and td/td; n= 7 for –/–) from 5 (WT), 2 (–/–) and 6 (td/td) different primary cell lines are shown. Student's t-test was applied, n.s., not significant.

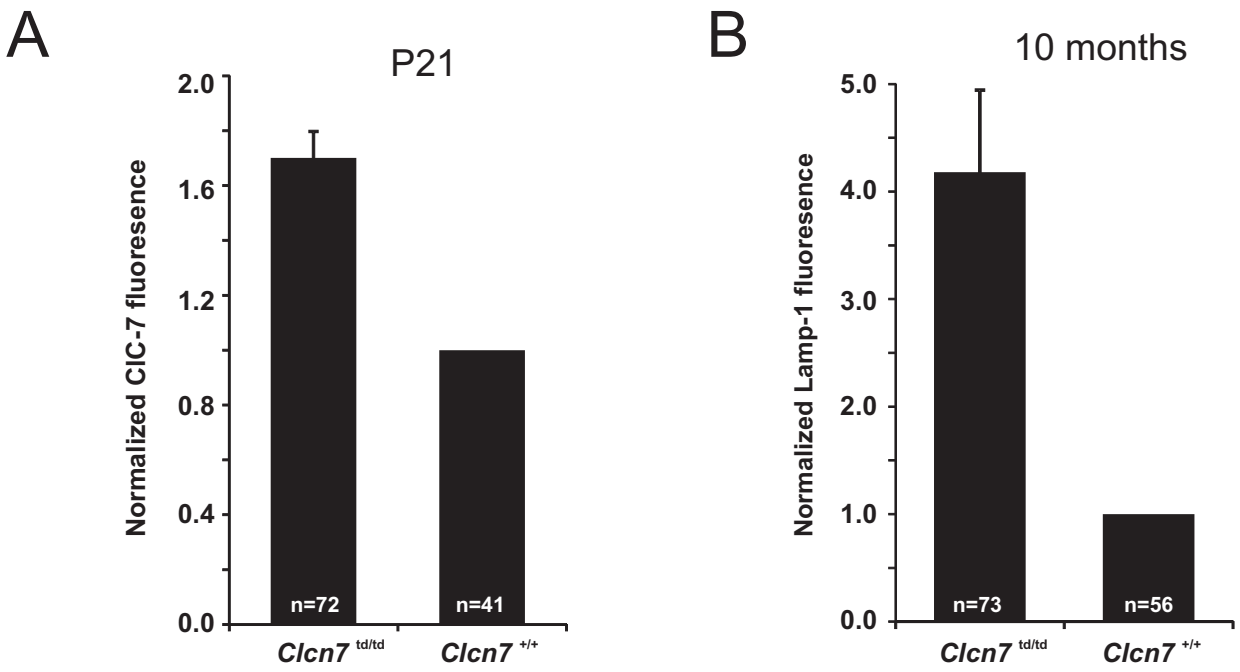

Figure E4. Quantification of abnormal lysosomal labelling. (**A**) About 70% increase of ClC-7 ^{td} fluorescence intensities in the somata of CA3 pyramidal neurons in *Clcn7* $^{td/td}$ mice compared to ClC-7 fluorescence intensities in *Clcn7* $^{+/+}$ mice at P21 (compare to main Figure 3A). Quantification was performed using ImageJ. A region of interest was placed around the cell bodies. Mean fluorescence intensities were determined and background subtracted. Quantifications were performed from 3 different animals per genotype including images shown in Figure 3. Normalization to images stained in parallel and acquired using identical settings. Total numbers of quantified cells are given. Error bars denote s.e.m. (**B**) Up to 4-fold increase of Lamp-1 fluorescence intensities in the somata of CA3 pyramidal neurons in *Clcn7* $^{td/td}$ mice at 10 months of age (compare to main Figure 3B). Autofluorescence of storage material which massively accumulates in lysosomal compartments in 10 months-old animals most likely contributes to the increased intensity. Quantification and normalization as in (A). Total numbers of quantified cells are given. Error bars denote s.e.m.

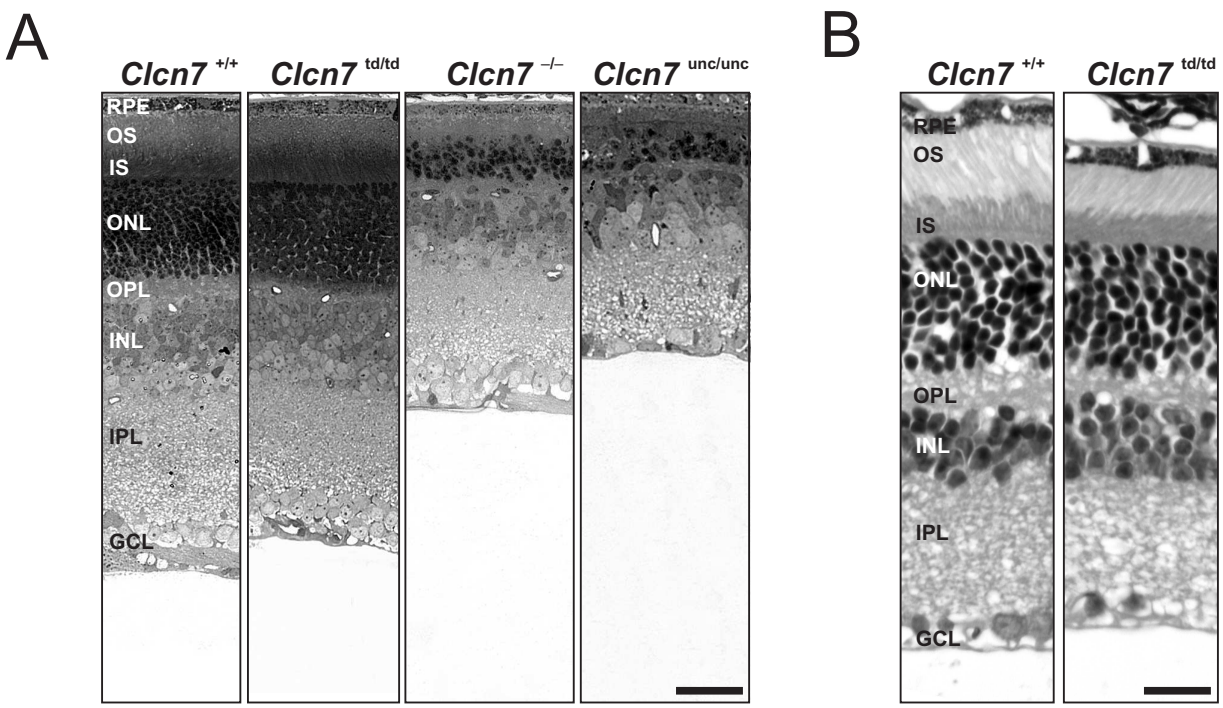

Figure E5. No retinal degeneration in *Clcn7*$^{td/td}$ mice. (**A**) Semi-thin sections of P28 retinae revealed degeneration of photoreceptor cells in the outer nuclear layer (ONL) and outer and inner segment (OS, IS, respectively) of *Clcn7*$^{unc/unc}$ and *Clcn7*$^{-/-}$, but not of *Clcn7*$^{td/td}$ mice (scale bar: 50 µm). (**B**) H&E staining on paraffin sections of the retina at 10 months of age. No obvious loss of photoreceptors in *Clcn7*$^{td/td}$ mice (n=2 animals each genotype). RPE, retinal pigment epithelium; OS, photoreceptor outer segments; IS, photoreceptor inner segments; ONL, outer nuclear layer; OPL, outer plexiform layer; INL, inner nuclear layer; IPL, inner plexiform layer; GCL, ganglion cell layer (scale bar: 100 µm).

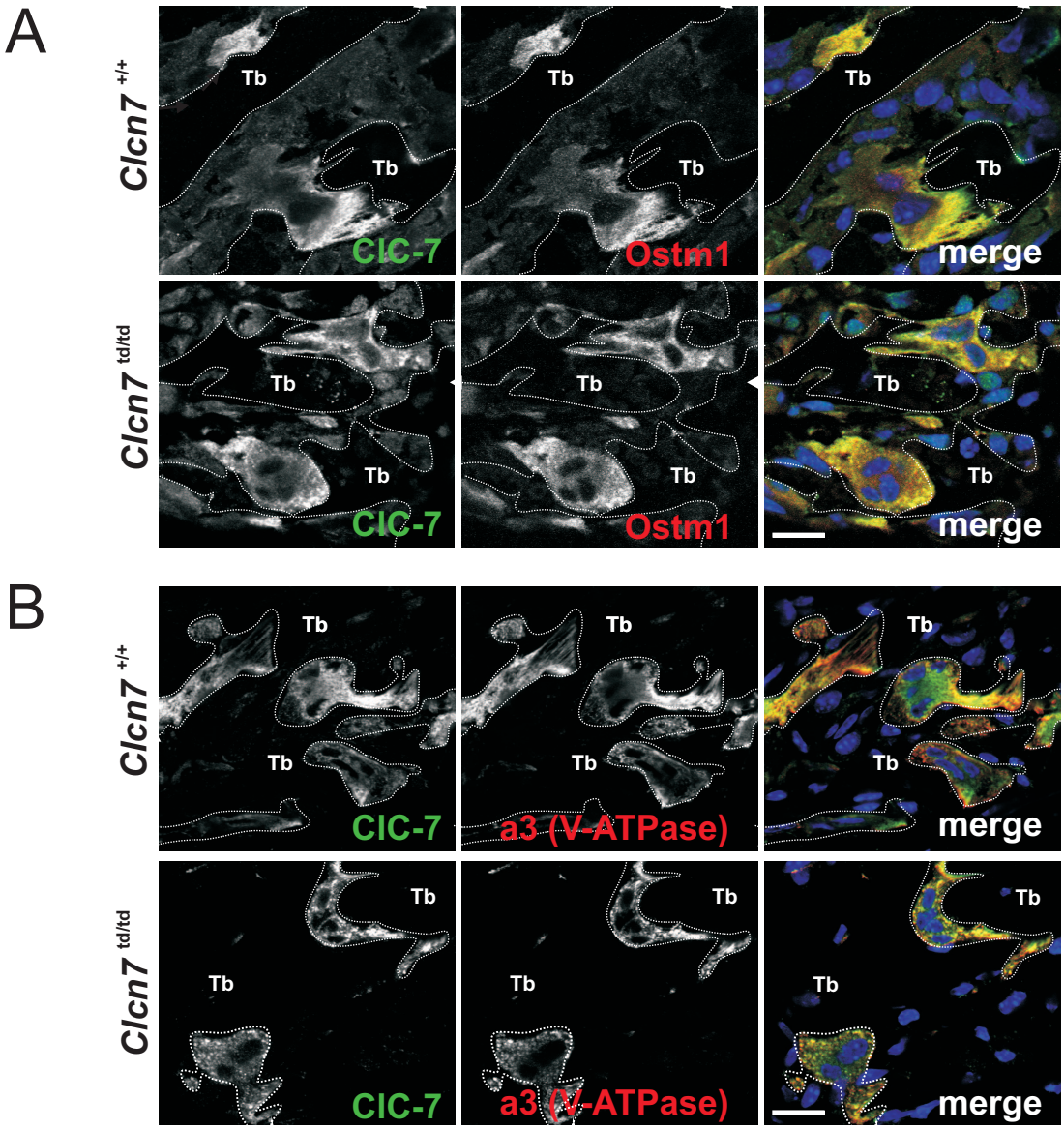

Figure E6. Localization of CIC-7^{td} and Ostm1 in *Clcn7*$^{td/td}$ tibia. (A) Immunostaining for CIC-7 (green) and Ostm1 (red) in bone. Both proteins showed dense overlapping staining in osteoclasts in areas that are partially opposed to trabecles (Tb) and represent ruffled borders (scale bar: 25 µm). (B) Co-localization of the a3 subunit of the V-ATPase (red) with WT CIC-7 and CIC-7td confirmed that both proteins were prominently found in the ruffled border and in intracellular compartments (dotted lines separate osteoclasts from bone tissue). DNA was stained with DAPI (scale bar: 25 µm).

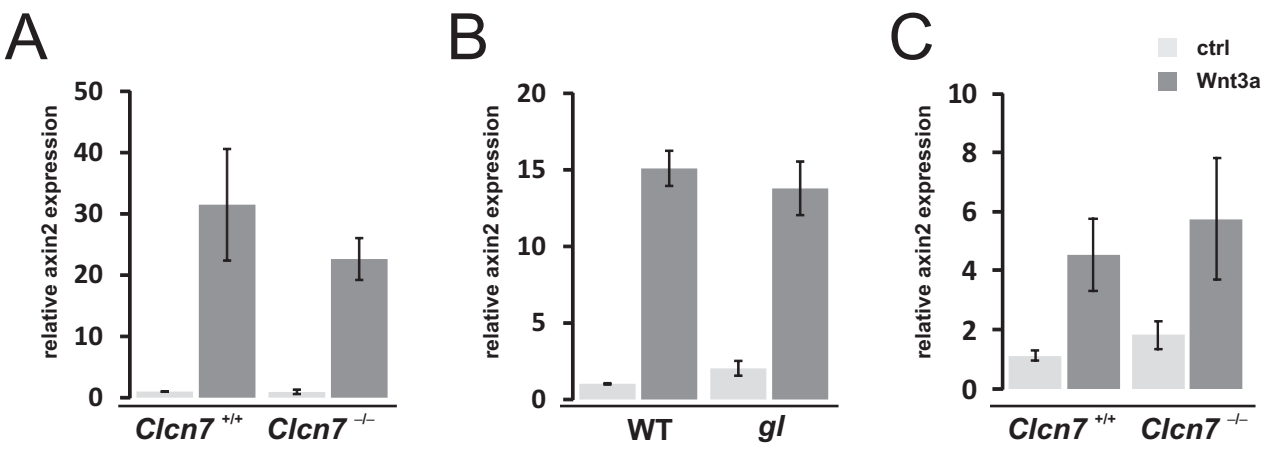

Figure E7. ClC-7/Ostm1-deficiency did not perturb Wnt signalling. WT and ClC-7-deficient (**A**) or gl (**B**) fibroblasts or WT and ClC-7-deficient melanocytes (**C**) were stimulated with rmWnt3a and expression levels of the Wnt target gene axin2 were determined by qRT-PCR. Experiments were performed with two (fibroblasts) and 6 (melanocytes) independent primary cell lines per genotype. Error bars denote s.e.m..

Expanded View

Mice

For the generation of *Clcn7*$^{td/td}$ mice 8 kb of mouse genomic sequence extending from exon 6 to 16 of *Clcn7* were amplified from R1 ES cells and cloned into pKO Scrambler plasmid 901 (Lexicon Genetics Incorporated) containing a dtA cassette (diphtheria toxin A cassette). A neomycin (neo) resistance cassette flanked by FRT sites was introduced between exon 7 and 8 to select for recombination in embryonic stem (ES) cells. Exon 11 was modified by insertion of the E312A mutation. The targeting construct was completely sequenced**.** Targeted R1 ES cells were screened by Southern blot analysis using *Bam*HI and an external 1.0-kb probe. Correctly targeted ES cells were injected into C57Bl/6 blastocysts. Chimeric animals were crossed with FLPe-recombinase-expressing 'deleter' mice and resulting heterozygous animals (*Clcn7*$^{+/td}$) were inbred to yield *Clcn7*$^{td/td}$. Exon 11 of the genomic *Clcn7*$^{td/td}$ gene was amplified with intronic primers and sequenced. Experiments were performed with mice in a mixed C57Bl/6-129/Svj genetic background, always using littermates as controls

Membrane preparation, tissue homogenates and immunoblot

For membrane preparation tissues were homogenized in PBS with protease inhibitors (Complete® protease inhibitor cocktail, Roche) and cleared two times by centrifugation at 1,000 x g for 10 min. Membranes were pelleted at 270,000 x g for 30 min and subsequently resuspended in PBS supplemented with protease inhibitors and 2% (w/v) SDS. For whole tissue homogenates organs were homogenized in PBS with 1% (v/v) NP-40 and protease inhibitors (Complete® protease inhibitor cocktail, Roche) and incubated for 30 min on ice. After centrifugation for 10 min at 20,800 x g the supernatant was used for SDS-PAGE. Equal amounts of protein were separated by SDS–PAGE and blotted onto nitrocellulose.

Histology and electron microscopy

Deeply anesthetized mice were perfused with 4% (w/v) PFA in PBS and isolated tissues were postfixed overnight at 4°C. Tibiae were decalcified for 4 days in 10% (w/v) EDTA in PBS and again postfixed. 3-µm paraffin sections of retina were used for H&E staining (old age), 8-µm paraffin sections of the brain were used for Nissl and periodic acid Schiff (PAS) staining and 8-µm cryosections for immunohistochemistry and lysosomal acid phosphatase assay. Lysosomal acid phosphatase activity *in situ* was determined using β-glycerophosphate as a substrate. Cryosections were incubated for 2 h at 37°C in 0.3% (w/v) sodium-β-glycerophosphate with 0.125% (w/v) lead nitrate in 50 mM acetate buffer pH 5.0. After washing, sections were stained with 0.1% (w/v) ammonium sulfide for 1 min. No staining was observed when substrate was omitted. For immunohistochemistry, sections were post fixed with 4% (w/v) PFA, permeabilized using 0.2% (v/v) Triton X-100 in PBS and blocked with 3% (w/v) BSA in PBS. Antibody incubation was in blocking buffer. For ClC-7, an antigen retrieval step (10 min in sodium citrate buffer, pH 6.0, at 95 °C) was included after fixation. For immunocytochemistry, fibroblasts were seeded onto glass coverslips, fixed for 12 min with 4% (w/v) PFA, treated with 30 mM glycine in PBS for 5 min, permeabilized with 0.1% (w/v) saponin and blocked with 3% (w/v) BSA in PBS. Confocal images were acquired with an LSM 510 (Zeiss) and ZEN software (Zeiss).

For electron microscopy, mice were perfused with 4% (w/v) PFA and 2.5% (v/v) glutaraldehyde in 0.1 M phosphate buffer (pH 7.4). Brains were cut in 150-µm sagittal sections with a vibratome. The eyes were opened at the crystalline lens and the vitreous humour removed. Tibiae were decalcified with 10% (w/v) EDTA in PBS for 3 to 4 days. Thin slices were prepared and postfixed in 2% (v/v) OsO_4, dehydrated and embedded in epon. Semi-thin sections (0.5 µm) were labelled with toluidine blue. Ultrathin sections (60 nm) were stained with uranyl acetate and lead citrate and examined with a Zeiss EM 902. Photographs were taken with a Megaview 3 Camera. Using the sealing zone as localization marker, the ruffled borders were graded *in situ* as absent, immature or mature with the experimenter blinded to the genotype.

Primary cell culture

Mouse adult fibroblasts from $Clcn7^{td/td}$, $Clcn7^{-/-}$ and WT mice were prepared by dissociation of tail biopsies with 0.2% (v/v) collagenase / 2U/ml dispase in PBS and cultured in DMEM containing 10% (v/v) fetal calf serum. Three independent cell lines from different animal were generated. For immunocytochemistry, fibroblasts were seeded onto glass coverslips and fixed. Melanocytes were isolated from dorsal skin of new-born pups by overnight dissociation of the epidermis in 0.25% Trypsin/EDTA solution (Life Technologies) at 4°C and cultured in melanocyte growth medium based on Ham's F12 (Life technologies) containing 20% (v/v) FBS, 1% (v/v) penicillin/streptomycin (both PAN-Biotech), 0.1 mM isobutylmethyl xanthine (Sigma-Aldrich), 10 µg/ml bovine pituitary extract (Life Technologies) and 48 nM 12-O-tetradecanoyl-phorbol-13-acetate (TPA, Sigma-Aldrich)

Determination of lysosomal pH

Lysosomal pH was measured by ratiometric fluorescence imaging of the pH sensor Oregon Green dextran 488 (Invitrogen) as described before . Primary cultures of fibroblasts were plated onto glass bottom life-cell dishes (MatTek) and loaded overnight with 0.5 mg/ml pH dye in growth medium. Cells were washed and Oregon Green dextran was chased into lysosomes for 2 h at 37°C in serum-supplemented growth medium. Ratiometric fluorescence images were acquired using an inverted microscope (Zeiss Axiovert 200 equipped with a 100x 1.30 NA oil immersion lens) connected to a Polychrom II monochromator (TILL photonics) at excitation wavelengths of 440 and 488 nm, respectively. The emitted light was filtered with a 535 ± 20-nm filter and captured with a Sensicam CCD camera (PCO). For each genotype, at least 3 different cells from 3 independent cell lines were measured in Ringer solution (in mM: 140 NaCl, 3 KCl, 2 K2HPO4, 1 CaCl2, 1 MgSO4, 5 HEPES, 10 glucose, pH 7.4). Image analysis was performed using a Fiji plug-in, in which regions of interest (ROI) were defined as areas above a defined fluorescence threshold in the acquired images at 488-nm excitation. The mean intensity ratio between 488- and 440-nm excitation was calculated for each ROI. At the end of each experiment, in situ pH calibration curves were obtained after treatment in isotonic K^+-based solutions (in mM: 5 NaCl, 115 KCl, 1.2 MgSO4, 10 glucose, 25 of either HEPES or MES, ranging in pH from 3.9 through 6.45) supplemented with 10 µM of both nigericin and monensin (both Sigma-Aldrich). Cells were equilibrated for at least 2 min for each pH value. The resulting fluorescence intensity ratio (488/440) as a function of pH was fit to a sigmoid and used to interpolate pH values from the experimental ratio data.

Determination of relative lysosomal chloride concentrations

Lysosomal chloride was measured by ratiometric fluorescence live cell imaging of MEQ/TMR-dextran (6-methoxy-N-ethylquinolinium iodide / tetramethylrhodamine-dextran) , that was targeted to lysosomes using a standard pulse-chase protocol. Primary cultures of fibroblasts were plated onto glass-bottom culture dishes (MatTek) and loaded for 1h with 20 mg/ml dye in growth medium. Cells were washed and MEQ/TMR-dextran chased into lysosomes for 2 h at 37°C in NaCl-reduced IMDM (Iscove's Modified Dulbecco's Medium; PAN-Biotech) with remaining [Cl^-] of 7 mM with NaCl substituted by Na-gluconate. Ratiometric fluorescence images at excitation wavelengths of 360 (MEQ) and 524 nm (TMR), respectively, were acquired using an inverted microscope (Zeiss Axiovert 200 equipped with a 100x 1.30 NA oil immersion lens) and an HC Tripleband Beamsplitter 403 497 574 (Semrock) connected to a Polychrom II monochromator (TILL Photonics) and a Lambda 10-2 emission filter wheel (Sutter Instruments). The emitted light was filtered with a 440 ± 20 nm (for MEQ) or 580 ± 20 nm filter (for TMR) and captured with a Sensicam CCD camera (PCO). For each genotype, 12 (+/+; td/td) or 7 (–/–) dishes with 10 different cells from 5 (+/+), 6 (td/td) or 2 (–/–) independent primary cell lines were measured in imaging buffer (in mM: Na-gluconate 135 mM Na-gluconate 5 KCl, 1 CaCl2, 1 MgCl2, 10 HEPES, 10 glucose, pH 7.4). Image analysis was performed with the Vision software package (TILL Photonics). For each cell, 10 lysosomes were chosen as regions of interest (ROI). The mean fluorescence intensity ratio between 360- and 524-nm excitation was calculated for each ROI after background subtraction.

Isolation of RNA and qRT-PCR

RNA was isolated from primary cells using the RNeasy mini kit (Qiagen) and transcribed to cDNA using SuperscriptII reverse transcriptase and random primers (Life technologies). qRT-PCR for axin2 was performed using RT² SYBR Green ROX qPCR Mastermix (Qiagen) with axin2-specific primers (forward: AGTCAGCAGAGGGACAGGAA; reverse CTTCGTACATGGGGAGCACT) in a StepOne Plus Cycler (Applied Biosystems). ß-Actin served as housekeeping gene (forward: tgtgatggtgggaatgggtcagaa; reverse: tgtggtgccagatcttctccatgt). The ΔΔCT method was used for analysis.

Supplementary Reference

Rodríguez CI, Buchholz F, Galloway J, Sequerra R, Kasper J, Ayala R, Stewart AF, Dymecki SM (2000) High-efficiency deleter mice show that FLPe is an alternative to Cre-loxP. *Nat Genet* **25:** 139-140